Depth estimation of pipe wall thinning using multifrequency reflection coefficients of T(0,1) mode-guided waves with supervised multilayer perceptron

Ryujin Katsuma[1], Koki Tada[1], Tomoya Iriguchi[1], Kotaro Seno[1], Shinsuke Kondo[1], Masashi Ishikawa[1], Motoki Goka[2], and Hideo Nishino[1]*

1) Tokushima University

2) Mitsubishi Chemical Co. Ltd.

* Corresponding author: hidero.nishino@tokushima-u.ac.jp

Depth estimation of pipe wall thinning using multifrequency reflection coefficients of T(0,1) mode guided waves with supervised multilayer perceptron

Abstract

This study entailed the development of a novel method for estimating the depth of wall thinning of pipes using multifrequency (30–65 kHz) reflection coefficients (MRCs) of the T(0,1) mode guided waves and a multilayer perceptron (MLP). First, this study established why MRCs are a critical feature of the input layer of the MLP for the defect depth estimation of wall thinning. Further, a mathematical model that can quickly collect large amounts of training data was used to calculate the reflection waveforms. The depths of artificial and actual wall thinning were estimated using the MLP based on the MRCs and the mathematical model. Experiments were conducted using the T(0,1) mode guided waves to obtain the MRCs for 21 artificial and 6 actual wall thinnings to estimate the defect depths. A maximum of 8347 training data points were prepared using the mathematical model. Because the optimization of the MLP strongly depended on the initial weights and biases, 100 random initial values were prepared to evaluate the average estimations and their standard deviations. The classification scheme of the MLP was used, with classification step widths of 0.5 and 0.25 mm. The correct answer rates for the 21 artificial defects were 93% with a tolerance of ±0.5 mm for the 0.5 mm classification scheme; those for the 0.25 mm classification scheme were 89%. For the six actual defects, the correct answer rates were 100% with a tolerance of ±0.5 mm for both the 0.5- and 0.25 mm classification schemes. Sufficiently high correct answer rates were obtained in all the cases.

1. Introduction

Guided wave inspection has been anticipated for the structural health monitoring (SHM) of piping in industrial and social infrastructures because it can cover long inspection ranges owing to its intrinsic capability of long-range propagation. One hundred meter propagation in actual chemical plant piping through butt welds and supports has been reported [1]. Guided wave theory was introduced [2] in 1959, and its first experimental verifications, notably in the dispersion relationships of the lowest two fundamental modes (the T(0,1) and T(0,2) modes), were conducted [3] in 1963. Several basic characteristics of guided waves in piping have revealed that the generation and detection efficiencies of the two lowest fundamental modes are similar to those of the Lamb waves in a plate [4]. Monographs [5,6] and textbooks [7] describing guided waves have been published.

SHM is fundamentally and conceptually different from nondestructive testing (NDT). SHM aims at real-time in-service automatic (without human judgments) diagnosis of the infrastructure; in contrast, NDT involves manual measurement and human assessment [8]. SHM generally requires three steps. These include (1) sensing and data collection using general-purpose signal processing, (2) feature extraction and selection, and (3) machine learning and assessment. In SHM, using a guided wave, time-domain signals are generally acquired using a piezoelectric sensor [9] or a magnetostrictive sensor [10] in step (1). These sensors are the de facto standards for transmitting and receiving guided waves for piping. After the aforementioned sensing process, noise reduction, envelope processing, frequency-domain signal processing, or a combination of these is applied to the received signals as part of step (1). Step (2) extracts and selects critical features to feed into the input layer for machine learning. However, among the features embedded in

the observed signals, the ones that are optimal for estimating the depth of wall thinning have not been identified. Hence, numerous approaches have attempted to identify critical features for extraction and selection. Time- and frequency-domain amplitudes, RMS, and their variances have been used in previous studies [11–14] as features for estimating the depth of wall thinning. In addition to the depth estimation of wall thinning, wavelet- or Hilbert-envelope time-domain signals have been widely used to estimate defect locations. These are simple methods for empirically determining critical features from well-known wave characteristic parameters. Genetic algorithms (GA) [15, 16] have also been utilized to extract and select critical features. The GA, which mimics the biological process of acquiring superior genes through generational change, is an optimizing method for obtaining the critical combination of features using selection, crossover, and mutation. Another important approach is to utilize matching pursuit (MP) [16–19], which is a greedy method for obtaining sparse signal representation (SSR) in an overcomplete dictionary. An overcomplete dictionary is a group of features that contain duplicate information. An SSR can be read as a representation containing only a few critical features in an overcomplete dictionary [20]. The extraction and selection of critical features using empirical and data-driven approaches (GA and MP) were used to determine the input data structure for the machine learning algorithm (MLA). Finally, in step (3), the MLA is applied to automatically estimate the wall thinning of the defect and other defect parameters [11-19]. Previous studies have demonstrated the significant potential of combining MLA and guided wave signals, yielding successful results. However, existing studies have focused on simple notched or slit geometries as defects without considering any variety of axial elongations. The actual wall thinning in piping typically involves gradual thinning, wherein the depth and axial extents of the thinning progress

simultaneously with the deterioration. When the depth and axial extents of wall thinning progress simultaneously, the signal amplitude does not increase linearly with the depth [21–26]. As such, it would be difficult to achieve an accurate estimation of defect sizing, even using the MLA. In this type of wall thinning, the signal amplitude of the guided wave changes as the axial length changes, even if the depth of the wall thinning is constant (Section 2). Experimental and theoretical observations indicate that the nonlinear relationship between the actual wall thinning and its signal amplitude depends primarily on the axial length of the wall thinning and is determined by the interference between two wave packets reflected from the front and rear ends of the wall thinning [21–25]. For example, realistic wall-thinning scenarios, such as those considering expansions in the axial and thickness directions, were excluded from the dataset due to challenges associated with size determination [14]. This is probably the main reason why the aforementioned studies were limited to simple notched or slit geometries.

This study proposes a novel method that uses a multilayer perceptron (MLP) with guided wave signals to estimate the depth of wall thinning in realistic defects that progress simultaneously in the axial and depth directions. This study showed that the depth of the wall thinning could be estimated using multifrequency reflection coefficients (MRCs) as a dataset for the input layer of the MLP. The importance of the MRCs for the depth estimation of realistic wall thinning is explained in Section 2. The cross-sectional loss (CSL) is widely used as an indicator of pipe deterioration. However, there can be high-risk pitting and low-risk shallow wall thinning at the same CSL value. Therefore, this study aimed to determine the maximum wall thinning depth, a field-required indicator.

This study presents a mathematical model [24, 26] used to obtain training data for a supervised machine learning system. The basic idea of the mathematical model is that the

reflection and transmission coefficients of the waveguide depend on the changes in the cross-sectional area of the medium [27]. The mathematical model used in this study can calculate the reflected waveform from any defect shape distributed axially along the pipe. In previous studies, the finite element method (FEM) was widely used to generate training data. However, FEM requires considerable time and is unsuitable for collecting training data. Regarding FEM or experimental data, the amount of training data for a supervised machine learning system has been limited from 10 to less than 100. Section 3 presents the details of the mathematical model and compares its calculation results to those of the large-scale FEM calculations. Section 4 presents the details and results of the guided wave experiments on artificial circular defects. The details of the MLP used in the verification and estimation results are also presented. Artificial circular defects are artificially created defects that mimic the shape of an actual thinning wall that partially emerges on a pipe surface. In Section 5, depth estimations using the MLP were demonstrated for six actual wall thinning in a chemical plant. In this study, a classification scheme was applied to the MLP. An important hyperparameter is the dropout rate for the MLP input layer, which is sensitive to the correct answer rate. This issue is discussed in Section 6. Section 7 presents the conclusion. This paper presents one of the first instances of the automatic estimation of actual wall thinning depths in 2B pipes, thereby achieving high accuracy through the application of an MLP.

2. MRCs as critical feature for MLP

This section explains why the MRCs are a critical feature for estimating the depth of wall thinning and why they are suitable as the input layer of the MLP. Using the shear horizontal (SH) plate wave as an example, the guided wave reflection phenomena are

described, especially highlighting the relationship between the defect length (concerning the propagation direction), the guided wave's reflection coefficient, and its frequency. The content concerning wave phenomena presented in this section is based on Figures 9 [21] and 14 [22] from original studies by Demma et al. Given its direct relevance to the current study, a concise overview is provided in this section.

The reflection coefficient of the SH-plate wave reflected at the rectangular notches as a function of the notch length in the propagation direction is shown in Figure 1(a). The notch depths for all the results were uniform, corresponding to 30% of the plate thickness. Two-dimensional (2D) FEM was used to obtain all the results (frequency=40 kHz and shear wave velocity=3120 m/s). The 2D FEM calculations were performed using ComWave[TM] (Ito-chu Techno Solutions Inc.) [28, 29]. The mesh geometry is square, each side is 0.5 mm long, and the total mesh count is 35880. The output of the simulation is wave displacement. The time-domain signals at notch lengths of 20 mm, 30 mm, and 40 mm are shown in the inset in Figure 1(a). The figure shows that the reflection coefficient varies considerably and is sometimes close to zero, even though the depth is the same. This suggests that it is impossible to quantify wall thinning with guided waves and that the presence of wall thinning may not even be detected. However, the aforementioned phenomenon occurs only for a single frequency. Figure 1(b) shows the reflection coefficient as a function of the frequency for a constant notch length of 40 mm. The inset in Figure 1(b) shows the time domain signals for three different frequencies. Using multiple frequencies can confirm the existence of non-zero reflection coefficients, thereby suggesting the possibility of quantitative measurements. Figure 2 shows 9 graphs of the reflection coefficient versus the frequency for different notch depths and lengths. Each graph was aligned horizontally with 20, 30, and 40 mm notch lengths and vertically with

10, 20, and 30% thinning depths to the wall thickness. The maximum reflection coefficients for the same notch depth remained unchanged, even when the notch length changed. In contrast, the maximum (even if the frequency at which the maximum value is taken changes) increased with the thinning depth. This is why we used MRCs as the input layer of the MLP, as they contribute to robust wall-thinning estimations for any defect length.

3. Mathematical model for calculating reflection signals at wall thinning

A large amount of high-quality training data is required to achieve high-accuracy supervised machine learning. However, obtaining these training data under various experimental conditions is almost impossible. In many previous studies, training data were obtained using the FEM. However, recent research has been limited to approximately 100 cases. This is because a large-scale FEM requires substantial computing power, thereby requiring a considerable amount of computing time. To solve the aforementioned problem, a mathematical model [24, 26] was used to calculate the waveform reflected from wall-thinning regions. Using this model, waveforms reflected at defects under different conditions can be obtained in large quantities at high speeds. The basic idea behind the mathematical model is that the reflection and transmission coefficients in the waveguide depend on changes in the cross-sectional area of the medium [27].

This section presents the mathematical model used to calculate the waveform reflected at wall thinning of an arbitrary shape. As is well known, the reflection and transmission at the boundary between the two bulk materials are represented by a specific acoustic impedance. Conversely, the reflection and transmission of the guided wave are

caused by the loss of its propagation medium. The reflection and transmission coefficients, $R_{0,1}$ and $T_{0,1}$, respectively, at an area change (from A_0 to A_1) of the propagation medium can be represented [27] using the characteristic acoustic impedances ($Z_0 = A_0 \rho c_t$ and $Z_1 = A_1 \rho c_t$) instead of the specific acoustic impedances, as follows:

$$R_{0,1} = \frac{Z_1 - Z_0}{Z_0 + Z_1} = \frac{A_1 - A_0}{A_0 + A_1}, \qquad T_{0,1} = \frac{2Z_1}{Z_0 + Z_1} = \frac{2A_1}{A_0 + A_1}, \tag{1}$$

where ρ and c_t are the density and shear wave velocity of the medium, respectively. In other words, the reflection and transmission coefficients can be represented using only their respective areas. Although the aforementioned calculation is for a single gap, the reflection waveform $u(t)$ for an arbitrary thinning shape can be expressed using Equation (2) (Figure 3) [24, 26]. This equation can be obtained by dividing the wall-thinning extent into microregions and summing their corresponding transmission and reflection coefficients, as expressed in Equation (2). The number of microregions, including those before and after wall thinning, was N.

$$u(t) = \sum_{n=1}^{N-1} \left\{ \left(\prod_{m=1}^{n-1} T_{m,m+1} \cdot T_{m+1,m} \right) R_{n,n+1} e^{2ink\Delta z} e^{-i\omega t} \right\}, \tag{2}$$

where i, k, Δz, ω, and t represent the imaginary number, wavenumber of the guided wave, length of the microregion, angular frequency, and time, respectively. Here, $\prod_1^0 = 1$. The amplitude of the incident wave was set as one. In Equation (2), the multiple reflections within the microregion and group of microregions are omitted as they are insignificant.

Because the mathematical model is a 2D model and is a method for calculating the waveform based on the distribution of the cross-sectional area change owing to wall thinning along the axial direction of the piping, information on the circumferential distribution of the defect is not included in the mathematical model. The reduction in the computation time is advantageous relative to the FEM. Although the calculation speed

was advantageous, it was slightly less accurate. Although the computed values of the mathematical model are inevitably less rigorous, they are conversely generalized or abstracted, which could be beneficial for the MLP training data. To evaluate the accuracy of the mathematical model, the 2D reflection coefficients calculated using the mathematical model were compared to those using the 3D FEM. The software [28, 29] used to calculate the 3D FEM was the same as that used for the 2D calculations in the previous section. The mesh geometry was cubic with a side length of 0.5 mm. The total number of meshes was approximately 22.3 million. The mathematical model was implemented in python. The step size for axial discretization (Δz) was set to 0.5 mm for the calculations. The wall-thinning shape for the verification is an artificial circular defect. Figure 4 shows photographs of the artificial circular defect on the 60.5 mm outer diameter and 3.9 mm thick steel pipe (2B Schedule 40) used in the laboratory tests and the geometry of the circular defect. Here, the parameter d represents the maximum depth, and r is the radius of the circular defect (see Figure 4). The parameter r is a quantity related to the axial extent of the wall thinning. The larger the r, the wider the wall reduction in the axial direction. In Figures 5(a)–5(i), the reflection coefficients calculated using the 3D FEM and mathematical model are shown for defect circular radii of 50, 100, and 200 mm and depths of 1, 2, and 3 mm. To quantitatively evaluate the difference between the two calculations, Equation (3) was used:

$$\text{Difference } = \frac{1}{36}\sum_{f=30}^{65}\frac{|FEM(f)-Math(f)|}{FEM(f)}, \tag{3}$$

where $FEM(f)$ and $Math(f)$ are the calculated reflection coefficients based on the FEM and mathematical model, respectively, and f represents frequency. Every evaluated value (percentage difference) is described in each graph of Figure 5. As shown in the figure, the difference increases with an increase in the radius of the circular defect.

11

The average differences for the three depths at the circular radii r = 50 mm and 100 mm are 11% and 21%, respectively. Hence, they are relatively close. Contrarily, when the circular radius r is 200 mm, the average difference reaches 46%. Unfortunately, the value is significant. This is because the FEM is a 3D model, and the mathematical model is a 2D model. Despite the aforementioned differences in the absolute values, there exist some similarities in the frequency characteristics of the reflection coefficients. In results (f), (h), and (i), the two calculations show similar characteristics, such as a relatively large reflection coefficient in the low-frequency region, which decreases toward the high-frequency region and peaks again. Finally, the engineering usefulness of the mathematical model must be evaluated using the estimation results of the MLP with the training data obtained from the mathematical model. This is particularly important when large amounts of training data are difficult to collect. The MLP evaluation results presented in later sections show accurate results in the cases for the circular radii r=50 mm and 100 mm. In comparison, the MLP with cases for the circle radius r=200 mm is rated high enough, although it is slightly lower.

4. Verification using artificial circular defects

4-1 Experiments

This section presents the experimental verification of the depths of artificial defects estimated using the MLP with the MRCs of the T(0,1) mode guided waves. A piezoelectric dry-coupled transducer [9] was used to generate and detect the T(0,1) mode guided waves. The sensor ring is manufactured in the laboratory and is made of aluminum alloy. It comprises nine shear vibration sensor elements that are installed evenly around the circumference of the pipe as one set. Two sets of them are supported on the sensor

ring and installed at 20 mm intervals in the axial direction of the specimen pipe. The selective transduction of the forward or backward propagation direction of the pipe was realized using the appropriate time-delay control of the input signals between the two sets; 4-cycle tone burst signals were used as the input waveforms. The frequencies of the $T(0,1)$ mode guided waves ranged from 30–65 kHz in steps of 1 kHz. The 60.5 mm outer diameter and 3.9 mm thick steel pipes (2B Schedule 40) with artificial circular defects were prepared for evaluation. The photographs and geometries of the artificial circular defects are shown in Figure 4. The experiments were conducted separately at two different times. In the first experiment, three different wall thicknesses (1.0, 2.0, and 3.5 mm) were prepared, and in the second, finer 0.5 mm steps of 3.5 mm. A lathe was used to create artificial circular defects with three different circular radii (r=50, 100, and 200 mm) on the specimen pipes. Eighteen different artificial circular defects were created, and the MLP was evaluated by estimating the defect depths.

The frequency variation (30−65 kHz) of the RF time-domain signals observed at the artificial circular defect (defect radius r=50 mm and depth d=2.5 mm) is represented as a typical signal, as shown in Figure 6. At every frequency, the launch signal is observed at 0.0 ms and the defect signal at approximately 0.5 ms. At around 65 kHz, ringing signals that extend after the launch signals can be observed. These signals are caused by the resonance of the circumferential Lamb waves generated just below the sensor. The mechanism of the resonant phenomena and its experimental verification have already been revealed in previous studies [30, 31]. The phenomenon principally depends on the number of sensor elements located evenly on the circumference [30, 31]. This spurious resonance is unwanted when detecting wall thinning, and it occurs in all of the present experiments because of its sensor dependence. For this reason, the upper limit of the

13

frequency range in all the experiments used here was set to 65 kHz. These spurious ringing signals can also be seen in the time domain signals shown in Figure 15. The reflection coefficients for the 6 defect depths (d=1.0~3.5 mm) as a function of the frequency are shown for the three circular radii (r=50, 100, and 200 mm) of the defects, as shown in Figures 7(a)–(c). In the low-frequency region, the deeper the defect or the smaller the defect radius, the larger the reflection coefficient. Contrarily, in the high-frequency region, the reflection coefficient tends to be smaller than that in the low-frequency region. Furthermore, it can be confirmed that the reflection coefficients sometimes switch between large and small values depending on the frequency. As shown in a later section, these phenomena have also been confirmed in actual wall thinning.

4-2 MLP details and training data preparation

Verifications were performed separately on the two MLP structures using the 0.5 mm step classification scheme (9 categories) and 0.25 mm step classification scheme (17 categories). The network architecture of the MLP for the 0.5 mm step classification scheme is illustrated in Figure 8. Four hidden layers are used. The input layer received the reflection coefficients of 36 frequencies (30–65 kHz). Regarding the input layer of the MLP, the frequency interval is 1 kHz in all the cases. These intervals were set relatively finely, although setting them sparsely may be necessary from a practical standpoint. This valid option contributes to simplicity and measurement speed in the field. Further study is needed for future work. In the 0.5 mm step classification scheme, the depth of the wall thinning was classified into 9 categories: 0.0, 0.5, 1.0, 1.5, 2.0, 2.5, 3.0, 3.5, and 3.9 mm. The 0.25 mm step classification scheme was classified into 17 categories, including 0.0–3.75 mm in 0.25 mm steps, along with 3.9 mm. The network architecture

parameters for both schemes are presented in Table I. Among the hyperparameters, the dropout rate to the input layer had a significant influence [32] on the estimation results. The backpropagation procedure was applied to the MLP to optimize the weights and biases of all the perceptrons using the Adam optimization algorithm [33]. The Adam hyperparameters are presented in Table III. The Adam parameters used here are the same as those recommended as the default values in the original study [33].

The training data were prepared separately for the 0.5 and 0.25 mm step classification schemes. The change in the cross-sectional area in the axial direction owing to a circular defect formed on the surface of a steel pipe with an outer diameter of 60.5 mm and wall thickness of 3.9 mm was calculated, from which the reflection waveform was finally calculated using Equation (2). The training data were prepared for artificial circular defects with radii ranging from 10–500 mm in 1 mm steps. The defect depths were the same as the depths used in the classification steps for the two classification schemes. The total training data for the 0.5 and 0.25 mm step classification schemes were 4419 and 8347 pieces, respectively. Each training dataset contained the reflection coefficients for 36 frequencies. As the number of classification steps increases, the required training data also increases. However, the mathematical model can rapidly calculate the training data, which addresses the increase in the training data. This is an advantage of the method that uses the mathematical model.

As presented in Tables I and II, dropout [32] was applied to the MLP. The dropout rate applied to the input layer contributed considerably to the correct answer rate, which is discussed in detail in the Discussion section. The initial values of the connection weights and biases for all the perceptrons are set randomly before applying the backpropagation procedure to optimize their values. The accuracy of the supervised

machine learning is strongly based on the initial weights and biases. Therefore, in our approach, the estimation results have been validated using 100 randomly generated initial values. The mini-batch method (mini-batch size of 350) was used for the Adam optimization procedure.

4-3 Estimation results

Figures 9(a) and (b) show the accuracy and loss versus the epoch for the artificial circular defects in terms of the 0.5 mm classification scheme, respectively. The blue lines in Figures 9(a) and (b) indicate the training accuracy and loss calculated using the training datasets computed using the mathematical model. The orange lines indicate the accuracy and loss (hereinafter referred to as test accuracy and test loss, respectively) calculated using all the MRCs obtained by the experiments of the 18 circular defects. A green line, as shown in Figure 9(a), shows the accuracy for defect depth with ±0.5 mm tolerance. The orange and green lines are accompanied by pale areas above and below them. These areas indicate the range of plus/minus one sigma obtained during 100 optimization trials for the weights and biases of the MLP from random initial values. The training accuracy and loss depicted by the blue lines also have pale areas, although they are too narrow to be seen in each graph. The solid line indicates the average value of each. Generally, some parts of the training data are split and used for validation calculations of the MLP. However, the experimental reflection coefficients were used as the validation data for network optimization to involve them in the optimization. We used the experimental reflection coefficients not only for defect depth estimation but also to validate the MLP. In other words, all the experimentally obtained MRCs were also used as validation data to determine the optimum epochs when the validation loss was minimized. As shown in

Figures 9(a) and (b), the training accuracy and loss monotonically increase and decrease, respectively, as the number of epochs increases. The test loss reached a minimum of 1.51 at 268 epochs. At 268 epochs, the test accuracy was 0.56, while the 0.5 mm tolerant accuracy was 0.94. After 268 epochs, the 0.5 mm tolerant accuracy slightly decreased, although high scores (>90%) were attained. Conversely, the test loss increased slightly with an increase in the number of epochs. This resulted in a gradual overfitting after 268 epochs. Figures 10, 11, and 12 show the classification results at 268 epochs for the experimental circular defects with radii of 50, 100, and 200 mm, respectively. The experiments were conducted using two different thinning steps. Each is indicated as Exp. 1 and Exp. 2 in the legends of Figures 10–12. The red vertical line in each graph indicates the correct defect depth. The error bars in each result indicate plus/minus one sigma for 100 estimation trials with random initial weights and biases. Because it is possible to confirm cases wherein the standard deviation is relatively large, in actual cases, two approaches can be applied: (1) the average estimate of at least ten trials may be obtained and evaluated in the actual operation, or (2) the optimal initial value obtained in advance may be used as transition learning. The estimation results for all the 27 separate experiments for the 18 different artificial circular defects are presented in Table IV. The overall percentages for the correct answers were 63% and 93% in ±0.5 mm tolerance, respectively. Overall, the estimated results generally corresponded with the correct depths of the artificial circular defects. In the ±0.5 mm tolerance, 100% correct answer rates were obtained in both cases for the defect circular radii of 50 and 100 mm. However, the correct answer rate for the 200 mm radius circular defects shows a high 7/9 (78%) in the 0.5 mm tolerant accuracy but a relatively poor 5/9 (56%) for the exact matches. As shown in Figure 5, the reflection coefficients as represented by the mathematical model do not

exactly correspond with the results of the FEM calculations especially for the 200 mm radius circular defects. This accounts for the relatively low estimated results. Further, the experimental reflection coefficients were relatively small in the circular defect with a radius of 200 mm than the other two circular defects (Figure 7), which may also have resulted in the aforementioned results.

Regarding the 0.25 mm classification scheme, the minimum loss was 2.06 at 136 epochs. At 136 epochs, the accuracy was 0.34, while the 0.25 and 0.5 mm tolerant accuracies were 0.73 and 0.90, respectively. Figure 13 shows the classification results of the 0.25 mm classification scheme with a circular radius of r = 50 mm at 136 epochs. The estimation results for all the evaluations are presented in Table IV, together with the results of the 0.5 mm classification scheme. The overall correct answer rates are 48%, 78% in ±0.25 mm tolerance, and 89% in ±0.5 mm tolerance, respectively. The exact match result is low, but this is inevitable due to the increase in the number of classification steps. The estimation results fairly corresponded with the correct depths, notably in ±0.25 and ±0.5 mm tolerances.

Compared to the 0.25 mm and 0.5 mm classification schemes (Figures 10 and 13), the positions of the peaks and the spreads of the distributions are considerably similar. In other words, although the overall correct answer rate is high, the correct answer rate is relatively low when the defect circular radius is 200 mm in the 0.25 mm classification scheme. This is the same reason described in the 0.5 mm classification scheme results.

5. Verification for actual defects of chemical plant piping

5-1 Actual defects and MRCs

In this section, the MLP is applied to 6 corrosion defects that are rusted on the

pipes of a chemical plant, and the estimation results of the defect depths are presented. The pipes are all 60.5 mm in outer diameter and 3.8 mm in wall thickness (2B SGP). The 6 corrosion defects are observed on the outer surface of the pipes. The 3D shapes of the 6 corrosion defects measured using a 3D laser scanner are shown in Figures 14(a)–(f). The maximum defect depths were 1.3, 1.5, 1.9, 2.1, 2.9, and 3.8 mm, respectively. The 3.8 mm depth implies a through-thickness hole. Four of the 6 defects (defect depths: 1.3, 1.9, 2.1, and 3.8 mm) were identified as single isolated corrosions. In the case of the 2.9 mm thinning depth, the 5 relatively large corrosions were clustered densely in a small area (approximately 40 mm in axial width), as shown in Figure 14(e). The last one, shown in Figure 14(b), has a maximum depth of 1.5 mm and is thinly distributed over a wide area. The distribution of fine corrosion clusters with large corrosion was confirmed in all the actual samples. The vertical axis in each graph indicates the circumferential location of the pipe, and the horizontal axis represents the axial distance from the piezoelectric dry-coupled transducer to the corrosion. The distances between the deepest point of corrosion and sensor location were 590, 970, 670, 490, 1355, and 980 mm (in decreasing order of the wall-thinning depth).

Guided wave experiments were performed to obtain the MRCs for the 6 actual corrosions. The tone burst signals were used to generate the T(0,1) mode guided waves, and the frequency range was from 30–65 kHz (1 kHz steps), which was the same as that used in the experiments for the artificial circular defects described in Section 4. The RF time-domain signals of the three corrosions (the maximum depths are 1.5, 2.1, and 3.8 mm) are shown in Figure 15. Each graph in Figure 15 represents a time-domain signal from a frequency of 30–65 kHz, which is arranged from bottom to top. The observed defect signal was normalized to the reflection signal at the end of the cutout piping to

obtain the reflection coefficient of the defect. The reflection coefficients for the two separate experiments for each of the 6 corrosion types as a function of frequency are shown in Figure 16. The reflection coefficients of the two deepest corrosions (d=3.8 mm and d=2.9 mm) were relatively high and easily distinguishable from those of the other 4 corrosions. For the latter group, which is smaller in size, the reflection coefficients for the deeper two corrosions (d=1.9 mm and d=2.1 mm) are larger than those for the shallower two (d=1.3 mm and d=1.5 mm) in the frequency range below 37 kHz. Above this frequency, the magnitudes of these coefficients are almost reversed. As highlighted in Section 2, this variability indicates the challenges in evaluating the depth of wall thinning using a single frequency. The MRCs obtained in this study were used as input signals for the MLP to estimate the defect depth.

5-2 Estimation results

Details of the MLP and other settings are the same as those of the artificial circular defects described in Section 4. It is intended to evaluate the versatile performance of this MLP by assessing artificial and actual defects in the same network architecture and hyperparameters (except for dropout rate).

The accuracy and loss as a function of epoch for the 0.5 mm step classification scheme are shown in Figures 17(a) and (b), respectively. The blue, orange, and green lines in Figure 17(a) represent the training accuracy, test accuracy, and 0.5 mm tolerant accuracy, respectively. The blue and orange lines in Figure 17(b) represent the training and test losses, respectively. All the lines and those accompanied by pale-colored areas are the average values and their ranges of the plus/minus one sigma taken during the 100 optimization trials (the standard deviations of the training accuracy and loss are too

20

minute to confirm, as shown in Figure 17). As described in Section 4-3, we used the experimentally observed MRCs not only for defect depth estimation but also for the validation of the MLP (it was used to determine the epoch at the minimum test loss). The test accuracy and loss owing to the actual defects have ideal characteristics—they are closer to the training accuracy and loss than those owing to the artificial circular defects, as shown in Figure 9. This suggests that the MLP network optimization for actual defects is more optimal than that for artificial circular defects; the estimation results are higher. It is suggested that the reflection coefficients produced by the mathematical model are closer to those of the actual defects rather than the artificial ones. When the number of epochs was 145, the test loss had a minimum value of 0.73. After 145 epochs, the test loss increased with the number of epochs, thereby confirming overlearning. At 145 epochs, the test accuracy and 0.5 mm tolerant accuracy are 0.70 and 1.00, respectively. Figures 18(a)–(f) show the estimated probabilities for the 6 actual defects at 145 epochs. The blue and orange bars in each graph represent the estimated probabilities for the same defect in two separate experimental results (Exp. 1 and 2). The red vertical lines in all the graphs represent the correct answers. All the estimation results correspond well with the correct depths of the actual wall thinning. Table V shows that the correct answer rate is 75% and that within ±0.5 mm tolerance is 100% for the 0.5 mm classification scheme.

Regarding the 0.25 mm classification scheme, the minimum loss was 2.00 at 120 epochs. At 120 epochs, the accuracy was 0.24, and the 0.25 and 0.5 mm tolerant accuracies were 0.70 and 0.95, respectively. The 0.25 mm tolerant accuracy of 0.70 is considered sufficiently practical. The estimated probabilities resulting from the two separate experiments for the 6 actual defects are represented by the blue and orange bars in Figures 19(a)–(f). Although the average correct answer rate was low at 25%, it was

21

considerably high at 75% for the ±0.25 mm tolerance and 100% for the ±0.5 mm tolerance. Table V presents the correct answer rates of the two classification schemes. High correct answer rates were obtained except for the exact accuracy of 25% for the 0.25 mm classification scheme. This is simply owing to the increased number of classifications. The results show higher percentages of correct answers with actual defects than with artificial circular defects, as compared to the description in Section 4. The low percentages of the correct answer rates for the artificial circular defects were for the case with a circular radius of 200 mm for wall thinning. In Section 3, it has been shown that for long axial thinning, the training data computed by the mathematical model do not agree well with the FEM data. The high estimation results obtained for the six actual defects may be due to the short equivalent axial lengths of the defects.

6. Discussion on dropout rate applied to input layer

Determining hyperparameters is a challenging problem in the construction of AI. In the proposed MLP, one example is "linear" instead of "relu" as the activation function of the input layer ("relu" was used in all the other hidden layers and "softmax" in the output layer (Table I)). One of the most important aspects found in our trial-and-error process was the application of dropout to the input layer of the MLP. The correct answer rate is highly susceptible to the dropout rate applied to the input layer. The application of dropout to the input layer can be interpreted as the result of an ensemble average [32] of applying multiple different MLPs, which has been shown to contribute to a higher correct answer rate. Figure 20 shows the accuracy as a function of the dropout rate to the input layer for the artificial circular defects in the 0.25 mm classification scheme. The orange bars represent the accuracy. Red and green bars represent accuracies in the ±0.25 mm and

±0.5 mm tolerances, respectively. The error bars represent the plus/minus one-sigma fluctuations for 100 trials with different initial weights and biases. The correct answer rate varied considerably based on the dropout rate. The accuracy changes from 0.05 to 0.34. In the ±0.25 mm tolerance, the accuracy changes from 0.20 to 0.75. In the ±0.5 mm tolerance, the accuracy varies from 0.52–0.91. In this section, the importance of the application of the dropout rate to the input layer has been confirmed. All the dropout rates used the values presented in Table II.

7. Conclusions

In this study, we developed a novel method for estimating the depth of wall thinning using an MLP that utilizes the MRCs of the T(0,1) mode guided waves. We devised an MLP-based method with a remarkably high percentage of correct answers. MRCs are a critical feature for estimating the defect depth of the MLP. They are necessary in identifying the defect depth when the axial size of the defect varies. Regarding the collection of training data, which is an important issue for supervised AI, a mathematical model was proposed and used to quickly obtain large amounts of training data. Up to 8347 different MRCs were used as training data. Quick and easy collections of large amounts of training data are the most important features of the mathematical model. The reflection coefficients of 36 frequencies (30–65 kHz) were used as the input layer of the MLP. Four hidden layers comprising 36, 700, 400, and 100 units were employed. Twenty-one types of artificial wall thinning that mimic actual wall thinning and 6 types of actual defects, which rusted and thinned in a chemical plant, were used to estimate the depth using the two classification schemes with different step widths (0.5 and 0.25 mm). The overall correct answer rates for the 21 artificial defects were 63% with an exact match

and 93% with a tolerance of ±0.5 mm in the 0.5 mm classification scheme. Those for the 0.25 mm classification scheme were 48% with an exact match, 78% with a tolerance of ±0.25 mm, and 89% with a tolerance of ±0.5 mm. Regarding the 6 actual defects of the chemical plant, the overall correct answer rates were 75% with an exact match and 100% with a tolerance of ±0.5 mm for the 0.5 mm classification scheme, while those for the 0.25 mm classification scheme were 25% with an exact match, 75% with a tolerance of ±0.25 mm, and 100% with a tolerance of ±0.5 mm. Sufficiently high accuracies were obtained within a tolerance of ±0.25 mm both in the artificial and actual defects. The findings of this study confirm that the dropout rate of the input layer is considerably influenced by improved correct answer rates. This study has presented a pioneering case in the automatic estimation of actual wall thinning depths using an MLP, thereby achieving high correct answer rates. This method has the potential to be easily adapted for various pipe sizes and classification categories, thereby allowing for the efficient preparation of extensive training data using the proposed mathematical model. Future studies will aim to validate this approach with a broader range of actual wall thickness reductions and different types of piping beyond 2B pipes. This study provides the basis for an automatic wall-thinning-depth estimation method, which is well-suited for SHM. The present method, along with the permanently installed sensors, has the potential to determine minute deterioration automatically.

Declaration of Conflicting Interests

The Authors declare that there is no conflict of interest.

Funding

References

[1] Cawley P, Lowe MJ, Alleyne DN, Pavlakovic B and Wilcox P. Practical long range guided wave inspection-applications to pipes and rail. *Mater Eval* 2003; 61(1): 66–74.

[2] Gazis DC. Three-dimensional investigation of the propagation of waves in hollow circular cylinders. I. Analytical foundation. *J Acoust Soc Am* 1959; 31(5): 568–573.

[3] Fitch AH. Observation of elastic–pulse propagation in axially symmetric and nonaxially symmetric longitudinal modes of hollow cylinders. *J Acoust Soc Am* 1963; 35(5): 706–708.

[4] Silk MG and Bainton KF. The propagation in metal tubing of ultrasonic wave modes equivalent to Lamb waves. *Ultrasonics* 1979; 17(1): 11–19.

[5] Rose JL. *Ultrasonic waves in solid media*. Cambridge: Cambridge University Press, 1999.

[6] Rose JL. *Ultrasonic guided waves in solid media*. Cambridge: Cambridge University Press, 2014.

[7] Royer D and Dieulesaint E. *Elastic waves on solids I*. Translated from original French edition. Heidelberg: Springer-Verlag, 2000.

[8] Mitra M and Gopalakrishnan S. Guided wave based structural health monitoring: A review. *Smart Mater Struct* 2016; 25(5): 053001.

[9] Alleyne DN and Cawley P. The excitation of Lamb waves in pipes using dry-coupled piezoelectric transducers. *J Nondestruct Eval* 1996; 15: 11–20.

[10] Kwun H and Bartels KA. Magnetostrictive sensor technology and its applications. *Ultrasonics* 1998; 36: 171–178.

[11] Rizzo P, Bartoli I, Marzani A and Lanza di Scalea F. Defect classification in pipes by neural networks using multiple guided ultrasonic wave features extracted after wavelet processing. *J. Pressure Vessel Technol* 2005; 127(3): 294–303.

[12] HosseinAbadi HZ, Amirfattahi R, Nazari B, Mirdamadi HR and Atashipour SA. GUW-based structural damage detection using WPT statistical features and multiclass SVM. *Appl Acoust* 2014; 86: 59–70.

[13] Hosseinabadi HZ, Nazari B, Amirfattahi R, Mirdamadi HR and Sadri AR. Wavelet network approach for structural damage identification using guided ultrasonic waves. *IEEE Trans Instrum Meas* 2014; 63(7): 1680–1692.

[14] Yaacoubi S, El Mountassir M, Ferrari M and Dahmene F. Measurement investigations in tubular structures health monitoring via ultrasonic guided waves: A case of study. *Measurement* 2019; 147: 106800.

[15] Acciani G, Brunetti G, Fornarelli G and Giaquinto A. Angular and axial evaluation of superficial defects on non-accessible pipes by wavelet transform and neural network-based classification. *Ultrasonics* 2010; 50(1): 13–25.

[16] Islam M, Sohaib M, Kim J and Kim JM. Crack classification of a pressure vessel using feature selection and deep learning methods. *Sensors* 2018; 18(12): 4379.

[17] Mallat SG and Zhang Z. Matching pursuits with time-frequency dictionaries. *IEEE Trans Signal Process* 1993; 41(12): 3397–3415.

[18] Hong JC, Sun KH and Kim YY. The matching pursuit approach based on the modulated Gaussian pulse for efficient guided-wave damage inspection. *Smart Mater Struct* 2005; 14(4): 548.

[19] Agarwal S and Mitra M. Lamb wave based automatic damage detection using matching pursuit and machine learning. *Smart Mater Struct* 2014; 23(8): 085012.

[20] Zhang GM, Zhang CZ and Harvey DM. Sparse signal representation and its applications in ultrasonic NDE. *Ultrasonics* 2012; 52(3): 351–363.

[21] Demma A, Cawley P, Lowe M, Roosenbrand AG and Pavlakovic B. The reflection of guided waves from notches in pipes: A guide for interpreting corrosion measurements. *NDT & E Int* 2004; 37(3): 167–180.

[22] Demma A, Cawley P, Lowe M and Roosenbrand AG. The reflection of the fundamental torsional mode from cracks and notches in pipes. *J Acoust Soc Am* 2003; 114(2): 611–625.

[23] Carandente R, Ma J and Cawley P. The scattering of the fundamental torsional mode from axisymmetric defects with varying depth profile in pipes. *J Acoust Soc Am* 2010; 127(6): 3440–3448.

[24] Nishino H. An investigation of reflection coefficients of the T(0,1) mode guided waves at axisymmetric defects and inverse problem analyses for estimations of defect shapes. *Mater Trans* 2015; 56(1): 120–128.

[25] Ishihara J, Ishikawa M and Nishino H. A mathematical model of the Lamb wave reflection at a two-dimensional rectangular notch. *Jpn J Appl Phys* 2019; 58(SG): SGGB08.

[26] Nagashima Y, Endou M, Miki M, Odakura M and Maniwa K. Defect sizing method using ultrasonic guided waves in pipes. *Rev. Prog. QNDE* 2009; 1096(1): 1583–1590.

[27] Choi MS, Kim SY, Kwun H and Light GM. Transmission line model for simulation of guided-wave defect signals in piping. *IEEE Trans Ultrason Ferroelectr Freq Control* 2004; 51(5): 640–643.

[28] Ikegami Y, Sakai Y and Nakamura H. A highly accurate ultrasonic simulator capable of over one billion elements for nondestructive evaluations. In *7th Int. Conf. on NDE,*

2009, 177–190.

[29] Furukawa T and Komura I. Simulation and visualization of guided wave propagation by large-scale 3D FEM, *EJ Adv Maint* 2011; 3(3): 92–101.

[30] Nishino H and Morita K. Resonant phenomena of circumferential Lamb waves by eight transducer elements located evenly on girth and wall thickness measurements, *40th Annual Review of Progress in Quantitative Nondestructive Evaluation. AIP Conf Proc.* 2014; 1581(1): 264–270.

[31] Nishino H, Iwata K and Ishikawa M. Wall thickness measurement using resonant phenomena of circumferential Lamb wave generated by plural transducer elements located evenly on girth. *Jpn J Appl Phys* 2016; 55(7S1): 07KC0.

[32] Srivastava N, Hinton G, Krizhevsky A, Sutskever I and Salakhutdinov R. Dropout: A simple way to prevent neural networks from overfitting. *J Mach Learn Res* 2014; 15(1): 1929–1958.

[33] Kingma DP and Ba JL. ADAM: A method for stochastic optimization. In: *International Conference on Learning Representations* (ICLR), 2015.

Figure Captions

Figure 1 Reflection coefficient of a rectangular notch as a function of the notch length in the propagation direction when the notch depth is 30% of the plate thickness (a) and as a function of frequency, wherein the notch length is 40 mm (b).

Figure 2 Nine variations in the reflection coefficients as functions of frequency. The 9 graphs correspond with changes in the notch length, 20, 30, and 40 mm, in the horizontal direction and the wall-thinning ratio, 10, 20, and 30%, to wall thickness in the vertical direction.

Figure 3 Arbitrary wall thinning is divided into microregion Δz along the axial direction. The waveform reflected at the wall thinning can be calculated by integrating the transmission and reflection coefficients at all the cross-sectional area changes while considering their corresponding phase advances.

Figure 4 Pictures of the artificial circular defect (slight top view and side view), and its geometry determined using two parameters d and r. Here, r=200 mm and d=3.5 mm.

Figure 5 Reflection coefficients of the artificial circular defects calculated using the FEM and mathematical model. The number in each figure indicates the difference between the results of the FEM and mathematical model calculations.

Figure 6 Frequency variation (30–65 kHz) of the time-domain signals observed with the artificial circular defect (circular radius r=50 mm and depth d=2.5 mm). The large signal at approximately 0.0 ms is the launch signal for each frequency. The signal at approximately 0.5 ms is the reflected signal at a circular defect.

Figure 7 Reflection coefficients of the artificial circular defects for the different depths as functions of the guided wave frequency. Circular radii of the defects are (a) 50, (b) 100, and (c) 200 mm, respectively. In all the cases, notably in the low-frequency range, deeper wall thinning results in a greater reflection coefficient, while in the high-frequency range, their relationship becomes more complex. These graphs indicate one of the reasons why defect depth estimation using guided waves of a single frequency is challenging.

Figure 8 Network architecture of the MLP used in the estimations.

Figure 9 Accuracy (a) and loss (b) as functions of the epochs for the artificial circular defects in the 0.5 mm classification scheme. At 268 epochs, when the loss is the

minimum at 1.51, the average accuracy and accuracy within ±0.5 mm tolerance are 0.56 and 0.94, respectively.

Figure 10 Classification results (estimated probability vs. defect depth) of the 6 artificial defects in the defect radius of 50 mm in the 0.5 mm classification scheme. Two estimation results based on the separate experiments are represented as the blue and orange bars for the defects of 1.0 mm, 2.0 mm, and 3.5 mm depths, while the other estimations are shown as only blue bars based on the single experiments.

Figure 11 Classification results for the 6 artificial defects in the defect radius of 100 mm in the 0.5 mm classification scheme.

Figure 12 Classification results for the 6 artificial defects in the defect radius of 200 mm in the 0.5 mm classification scheme.

Figure 13 Classification results (estimated probability vs. defect depth) for the six artificial defects in the defect radius of 50 mm in the 0.25 mm classification scheme.

Figure 14 Defect depth distributions for the 6 actual defects thinned in a chemical plant. The 3D laser measurements revealed the actual defect distributions.

Figure 15 RF time-domain signals of the multifrequency (30–65 kHz) observed for the 3 actual defects.

Figure 16 Frequency variation of the reflection coefficients for the 6 actual defects. Two separate experimental results are shown for every 6 defects.

Figure 17 Accuracy (a) and loss (b) as functions of the epochs for the 6 actual defects in the 0.5 mm classification scheme. At 145 epochs, when the loss value is a minimum of 0.70, the accuracy and accuracy within ±0.5 mm tolerance are 0.70 and 1.00, respectively.

Figure 18 Classification results of the 6 actual defects in the 0.5 mm classification scheme.

Figure 19 Classification results of the 6 actual defects in the 0.25 mm classification scheme.

Figure 20 Accuracy and accuracies within ±0.25 mm and ±0.5 mm tolerances as a function of the dropout rate of the input layer for the artificial circular defects in the 0.25 mm classification scheme. The accuracy changes significantly with the changes in the dropout rate. Table II summarizes the dropout rates applied to the input layer in this study.

Table Captions

Table I MLP architecture details for the 0.25 mm and 0.5 mm step classification schemes.

Table II Dropout rate at the input layer.

Table III Adam parameters for the network optimization.

Table IV Summary of the estimation results for the artificial circular defects.
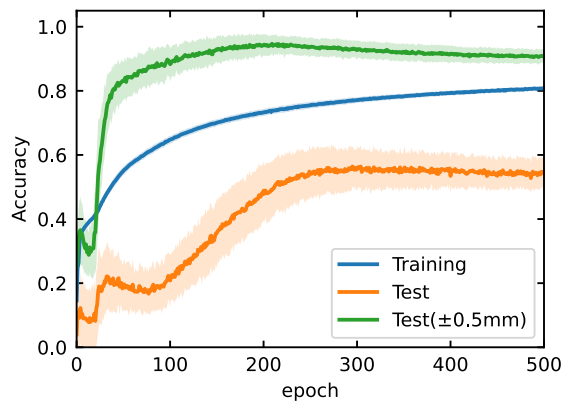
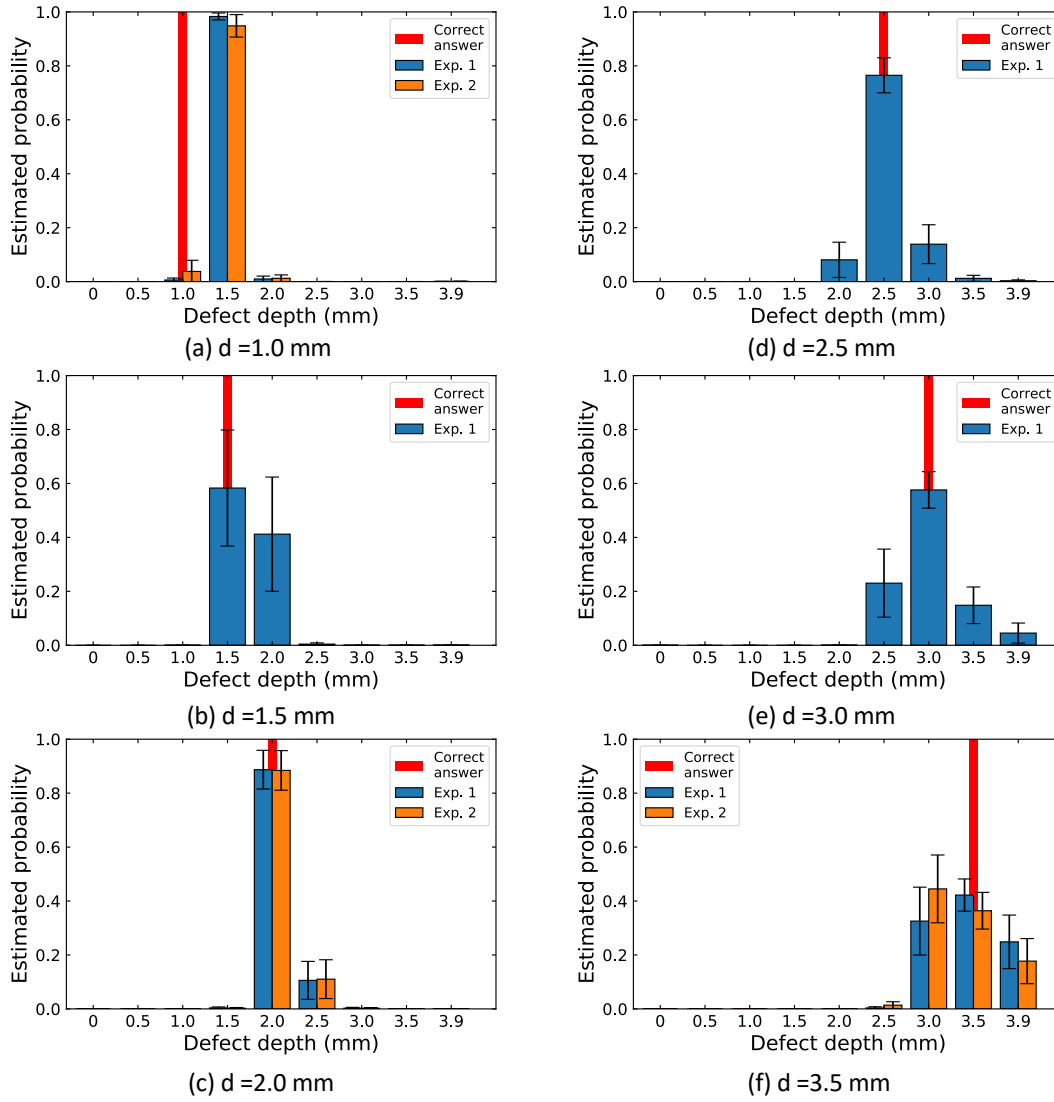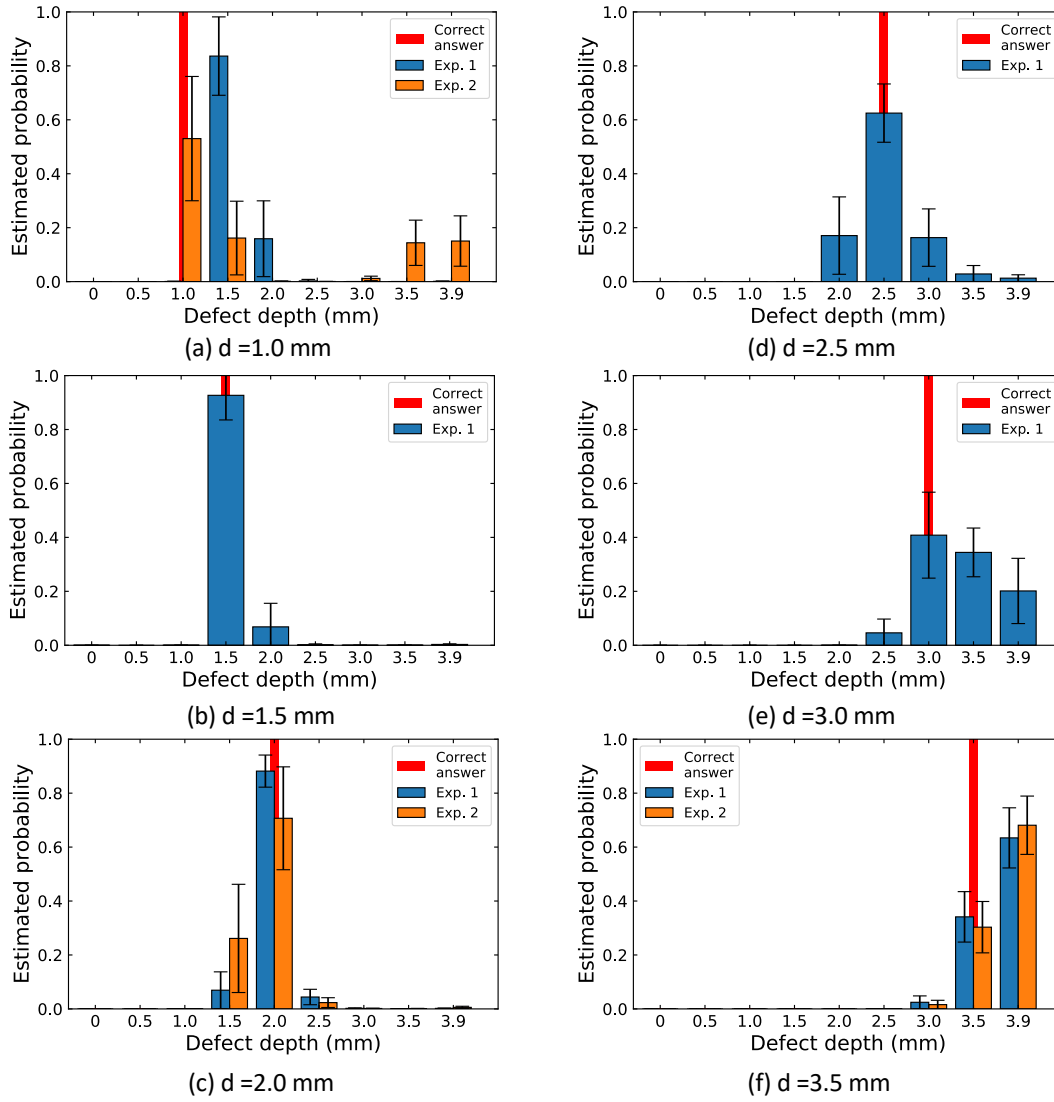Table V Summary of the estimation results for the actual defects.
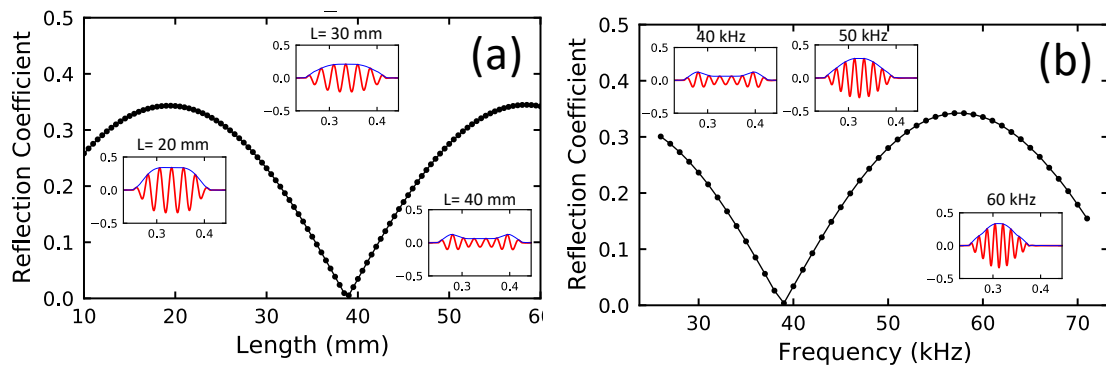
Figure 1

R. Katsuma et al
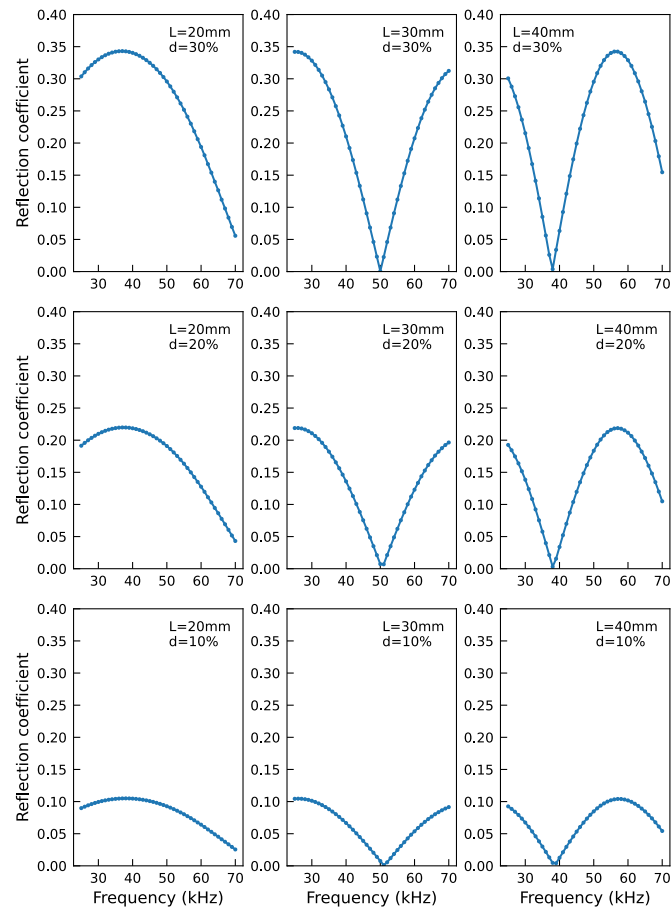
Figure 2

R. Katsuma et al

Figure 3 R. Katsuma et al

Circular radius
r = 200 mm

Depth
d = 3.5 mm

Defect-
geometry and two parameters, r and d.

expanded

Side view

Slight top view

Figure 4 R. Katsuma et al

(a) r=50 mm, d=1.0 mm

(b) r=100 mm, d=1.0 mm

(c) r=200 mm, d=1.0 mm

(d) r=50 mm, d=2.0 mm

(e) r=100 mm, d=2.0 mm

(f) r=200 mm, d=2.0 mm

(g) r=50 mm, d=3.0 mm

(h) r=100 mm, d=3.0 mm

(i) r=200 mm, d=3.0 mm
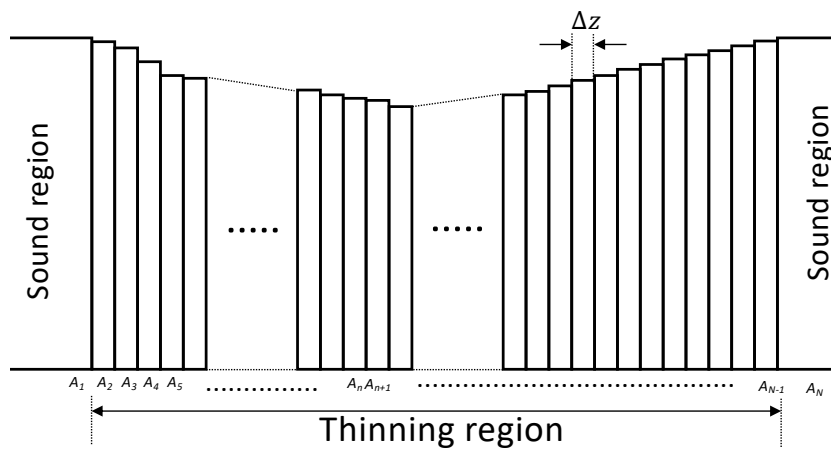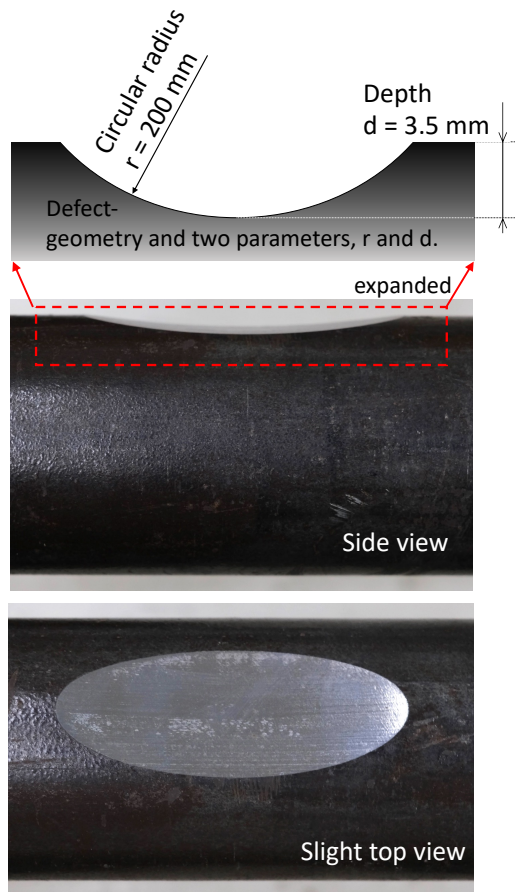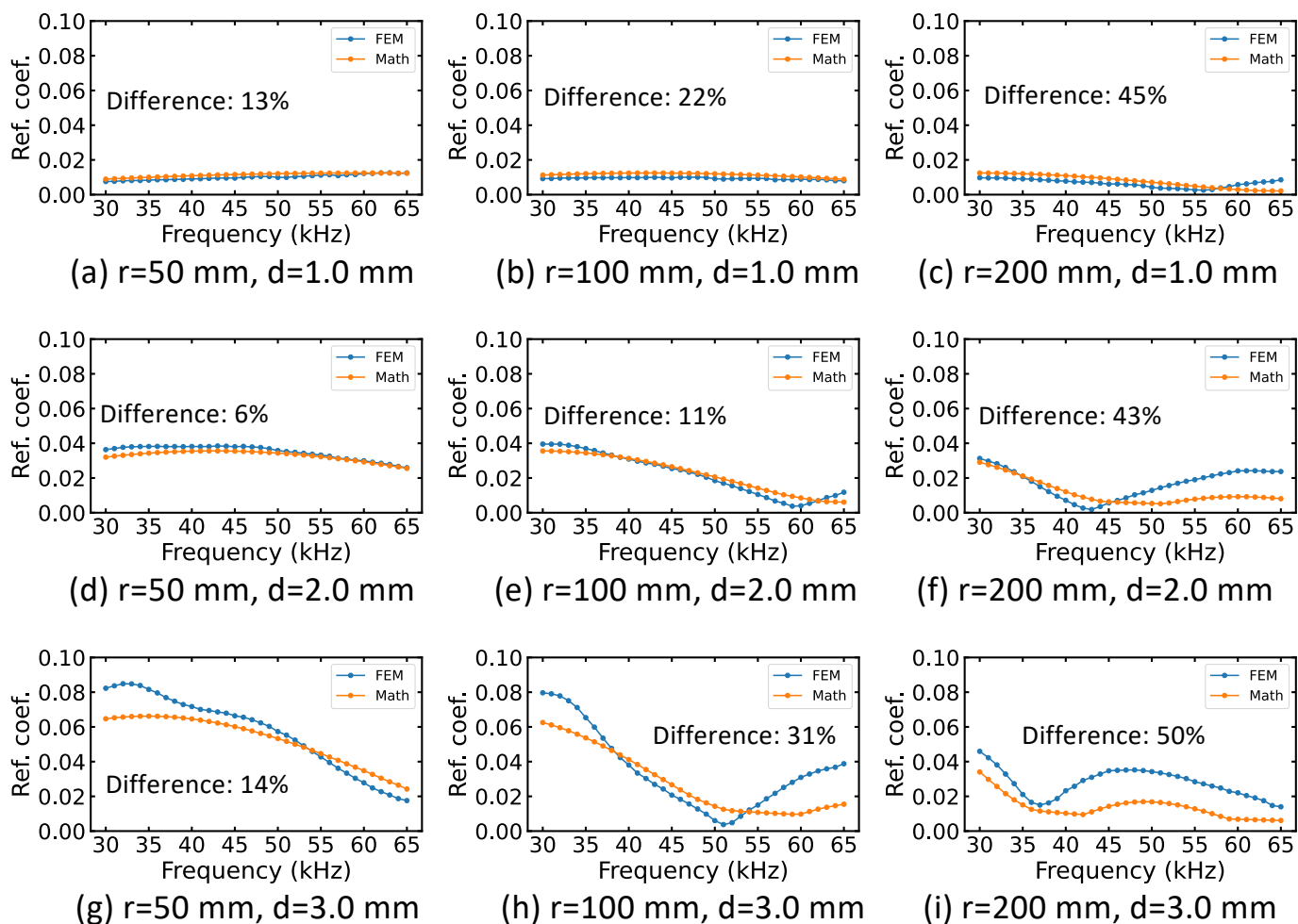
Figure 5
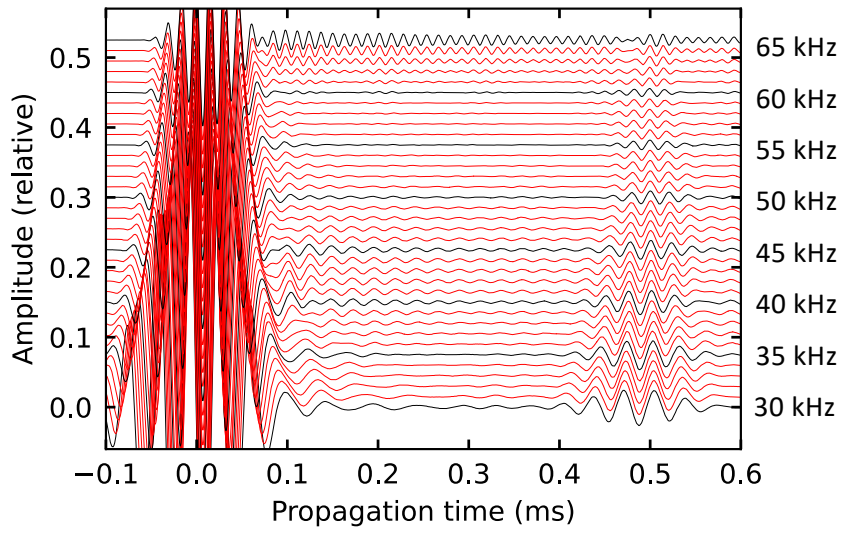
R. Katsuma et al

Figure 6

R. Katsuma et al

R50mm, d2.5mm
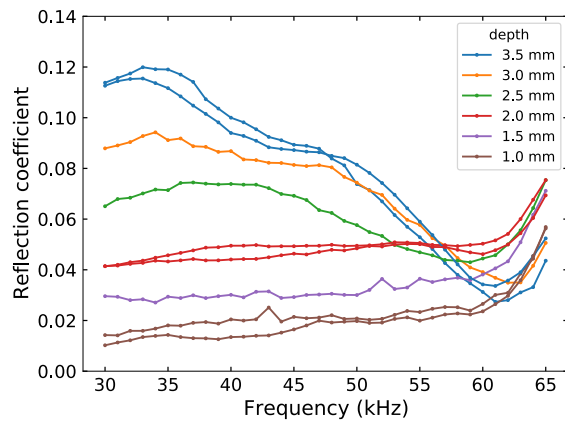
(a)
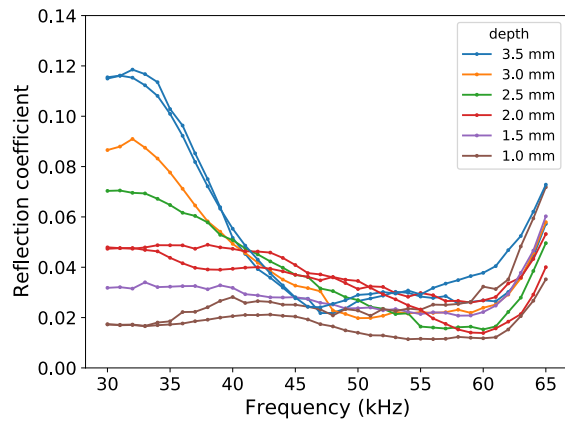
(b)
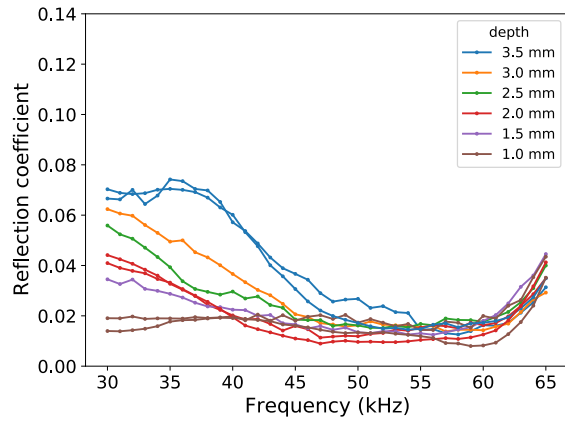
(c)

Figure 7

R. Katsuma et al
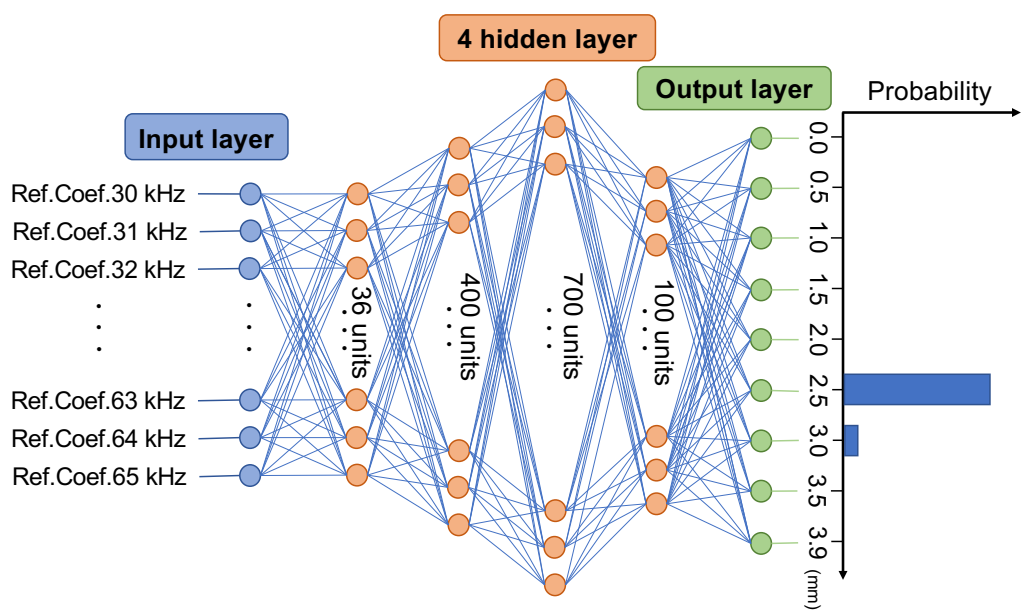
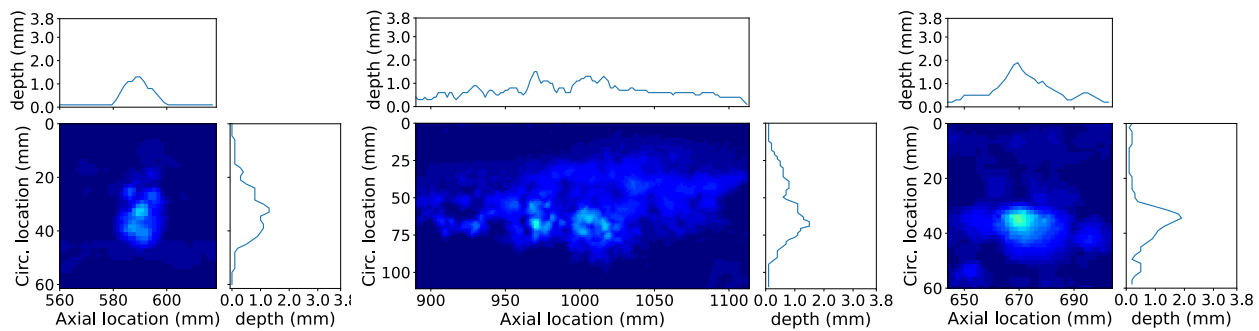Figure 8

R. Katsuma et. al.

(a)

(b)

Figure 9

R. Katsuma et. al.

(a) d =1.0 mm

(b) d =1.5 mm

(c) d =2.0 mm

(d) d =2.5 mm

(e) d =3.0 mm

(f) d =3.5 mm

Figure 10

R. Katsuma et. al.

(a) d =1.0 mm

(b) d =1.5 mm

(c) d =2.0 mm

(d) d =2.5 mm

(e) d =3.0 mm

(f) d =3.5 mm

Figure 11

R. Katsuma et. al.

(a) d =1.0 mm

(b) d =1.5 mm

(c) d =2.0 mm

(d) d =2.5 mm

(e) d =3.0 mm

(f) d =3.5 mm
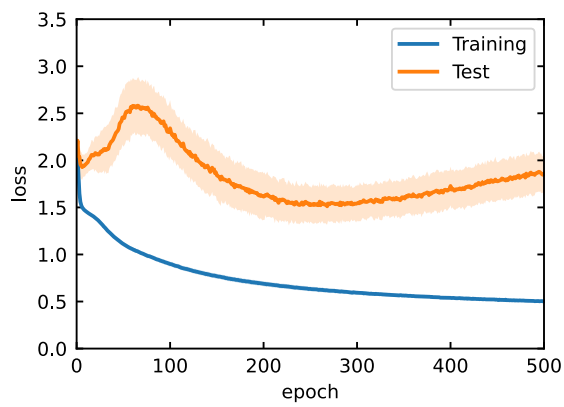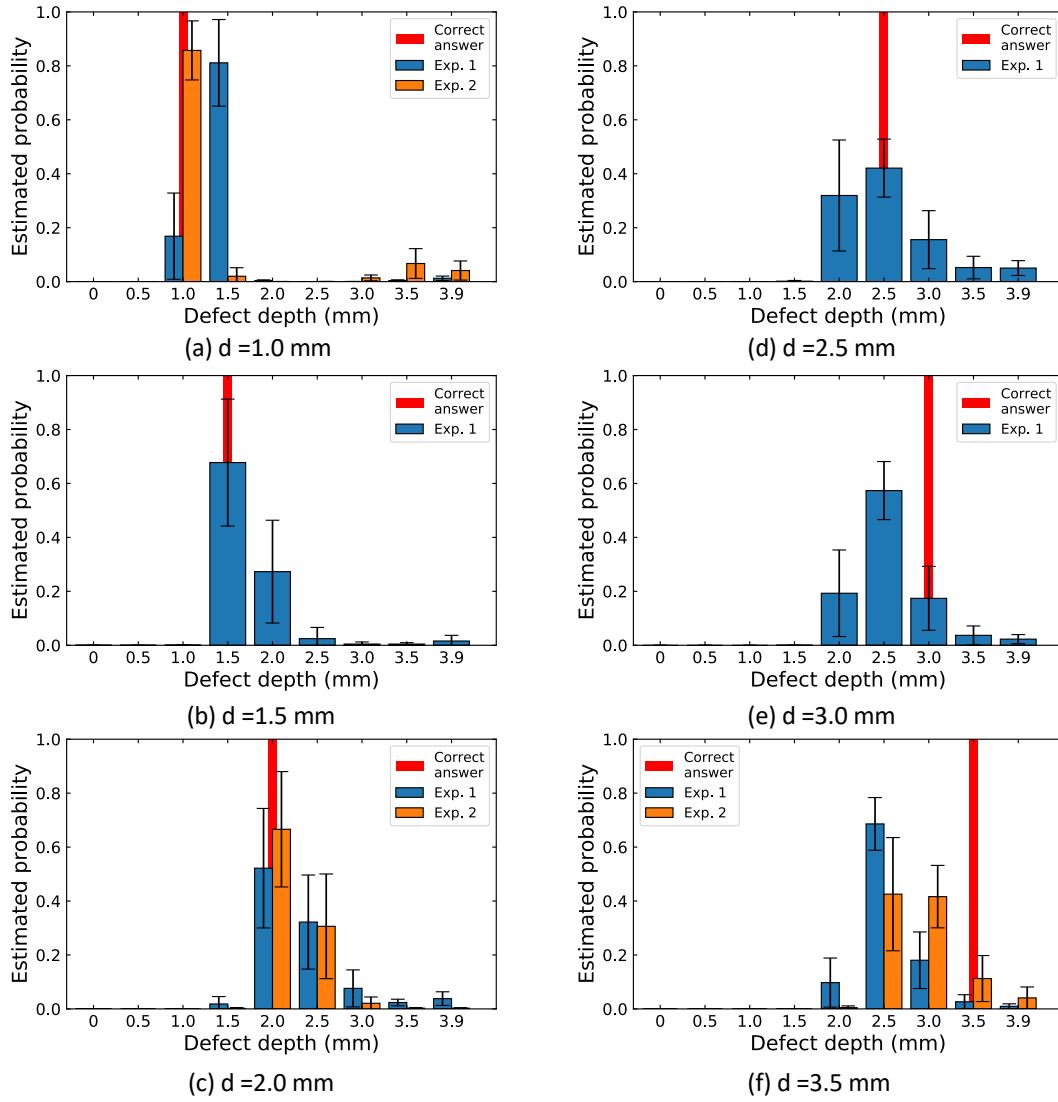
Figure 12

R. Katsuma et. al.

(a) d =1.0 mm

(b) d =1.5 mm

(c) d =2.0 mm

(d) d =2.5 mm

(e) d =3.0 mm

(f) d =3.5 mm
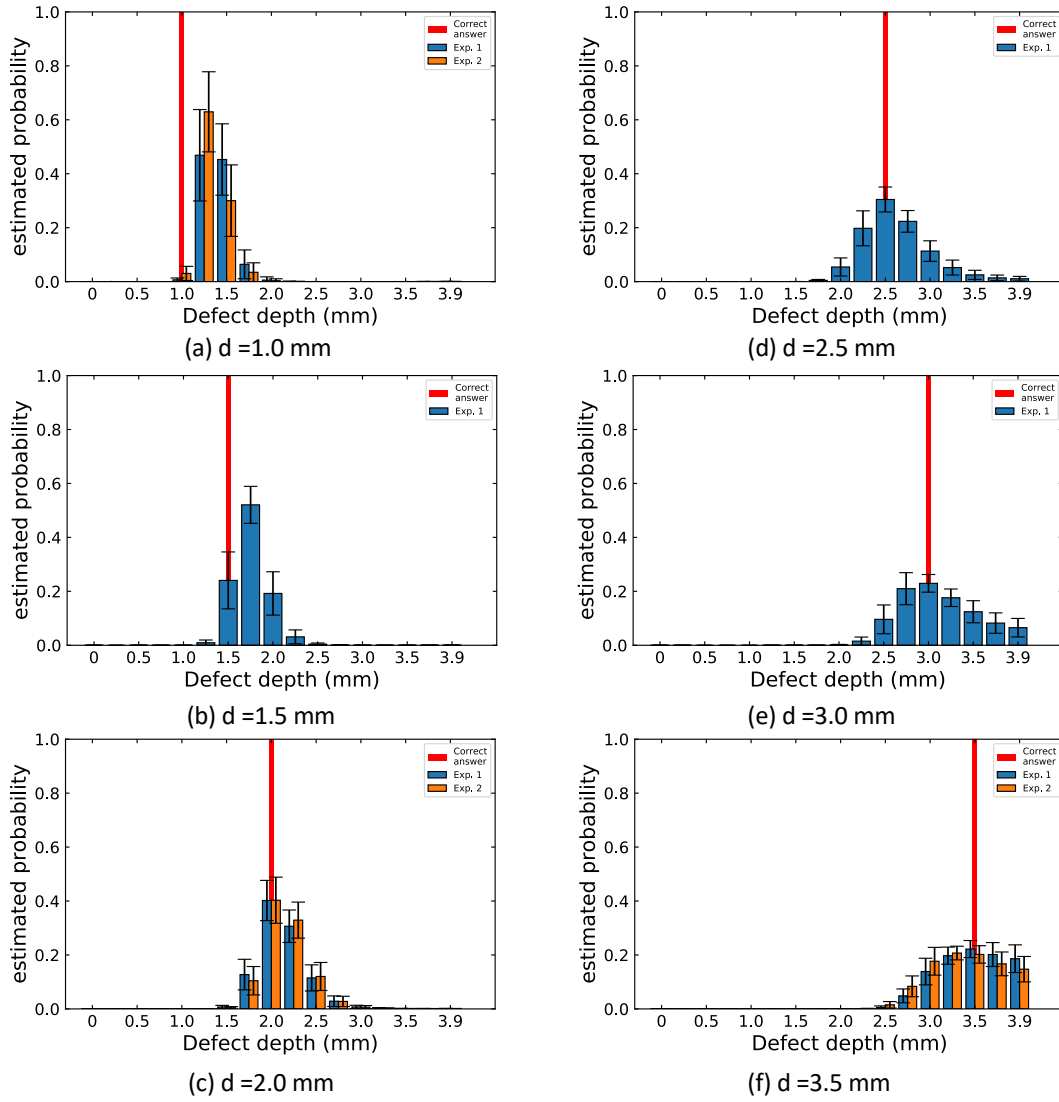
Figure 13

R. Katsuma et. al.

(a) Max. depth = 1.3 mm

(b) Max. depth = 1.5 mm

(c) Max. depth = 1.9 mm
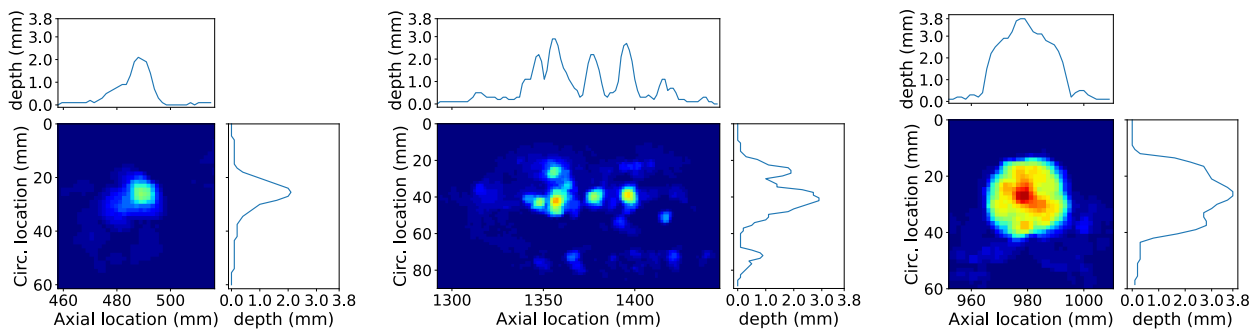
(d) Max. depth = 2.1 mm

(e) Max. depth = 2.9 mm

(f) Max. depth = 3.8 mm
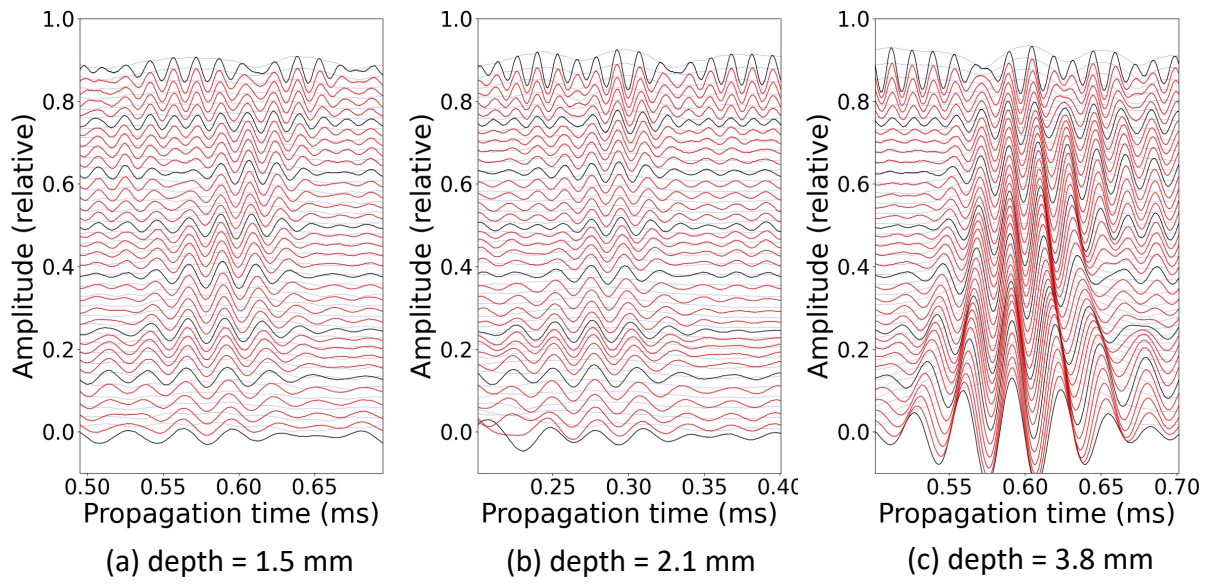
Figure 14

R. Katsuma et. al.

(a) depth = 1.5 mm   (b) depth = 2.1 mm   (c) depth = 3.8 mm
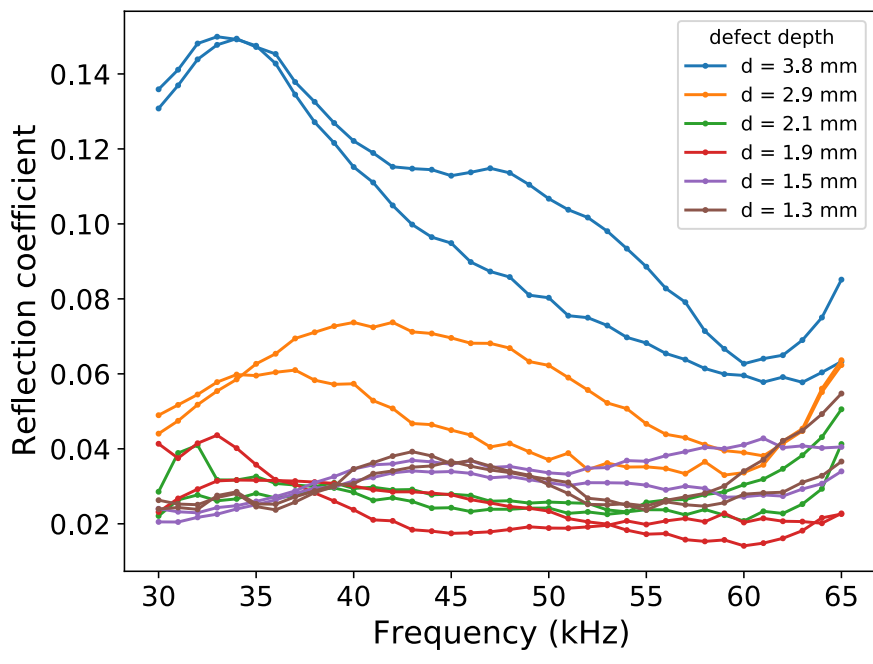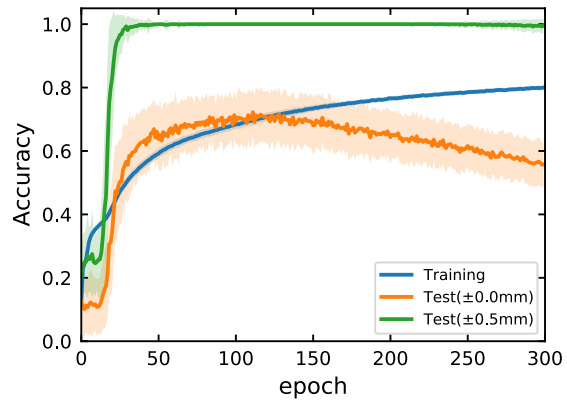
Figure 15

R. Katsuma et. al.

Figure 16

R. Katsuma et. al.
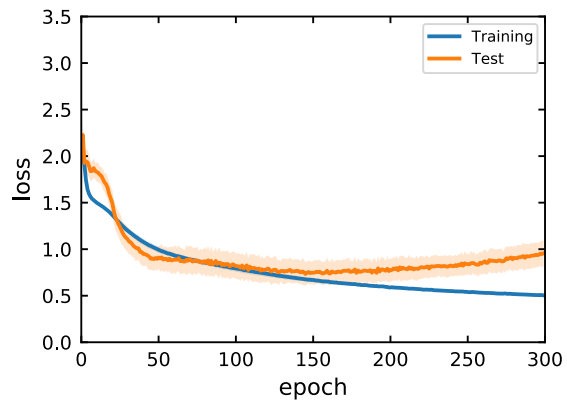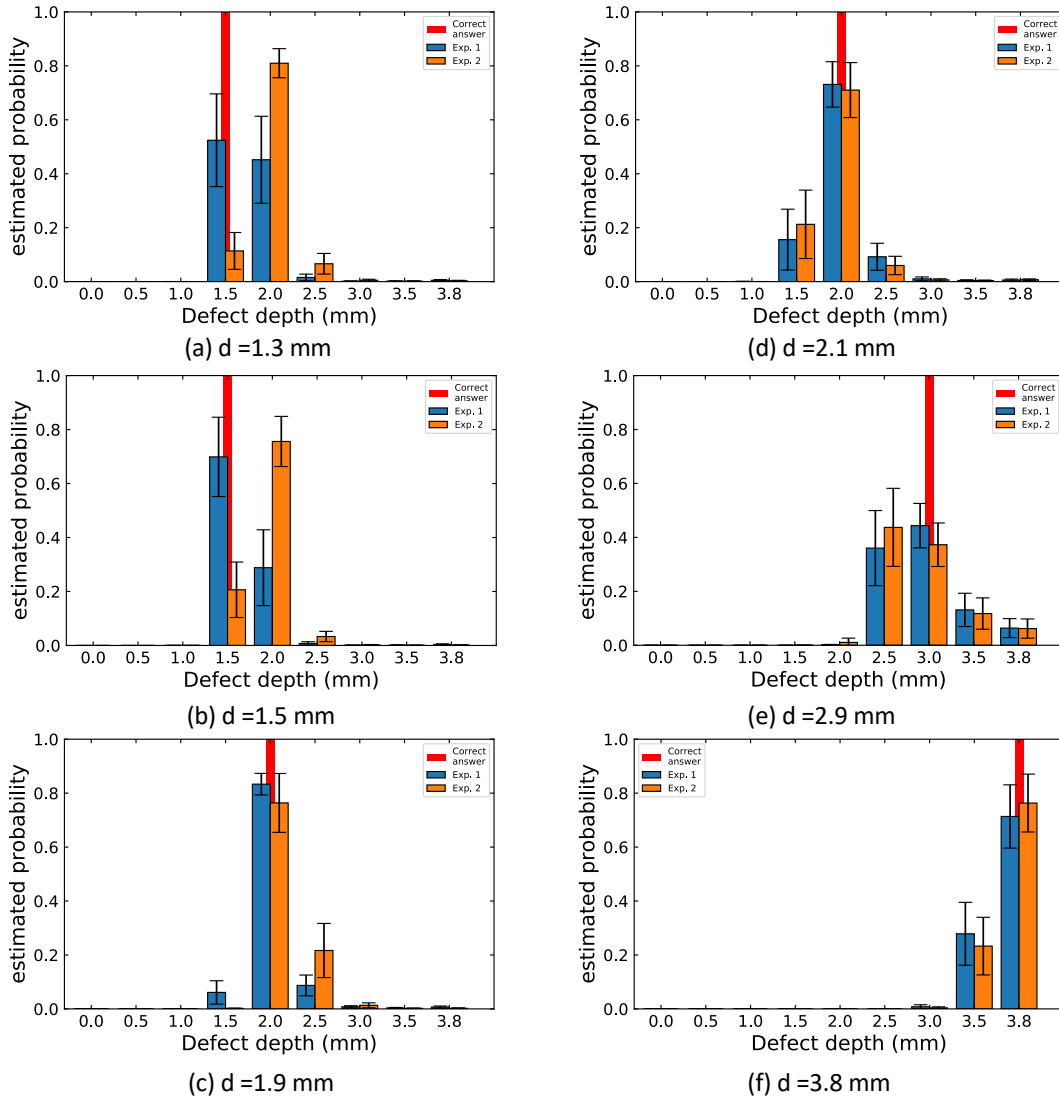
(a)

(b)

Figure 17

R. Katsuma et. al.

(a) d =1.3 mm

(b) d =1.5 mm

(c) d =1.9 mm

(d) d =2.1 mm

(e) d =2.9 mm

(f) d =3.8 mm

Figure 18

R. Katsuma et. al.

(a) d =1.3 mm

(b) d =1.5 mm

(c) d =1.9 mm

(d) d =2.1 mm
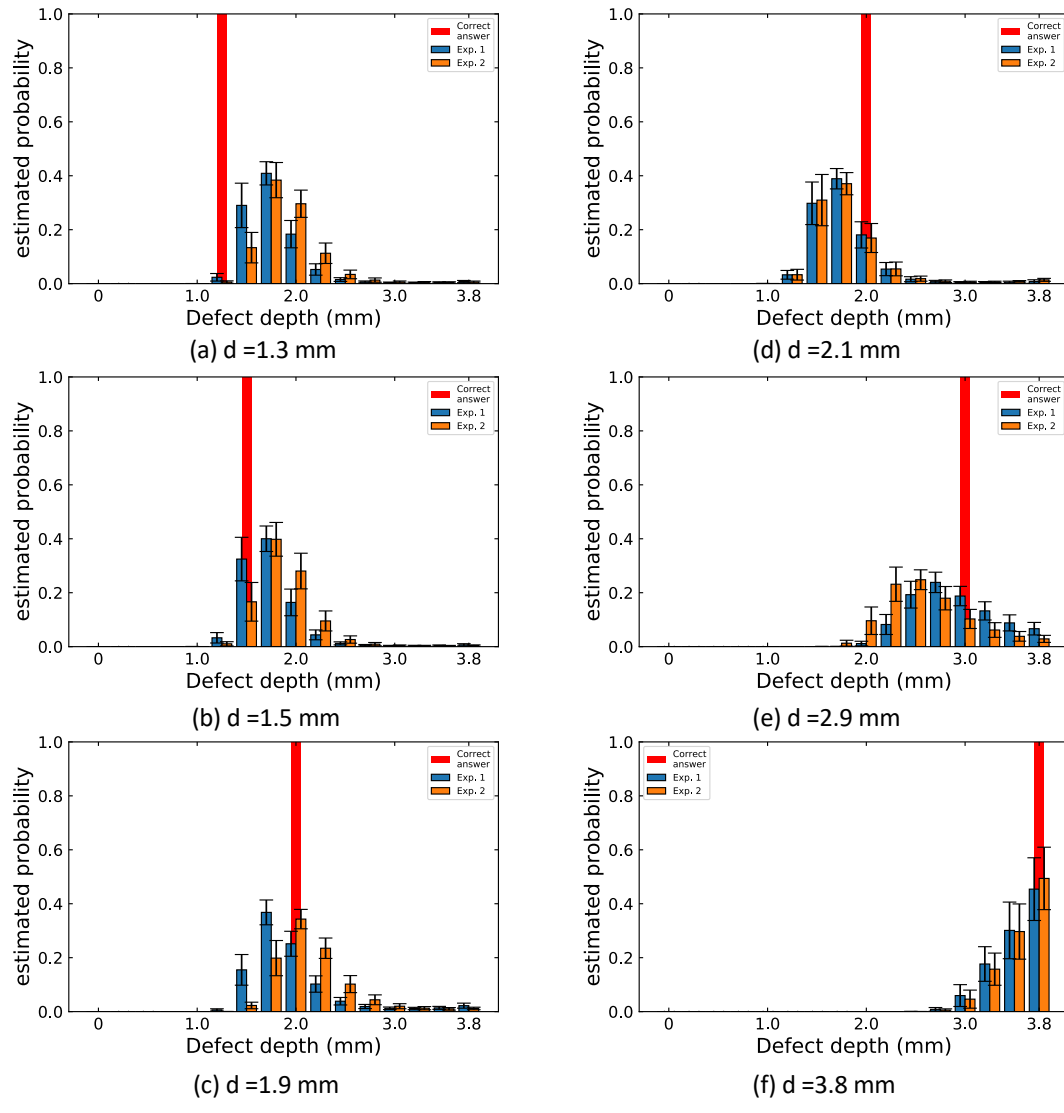
(e) d =2.9 mm

(f) d =3.8 mm
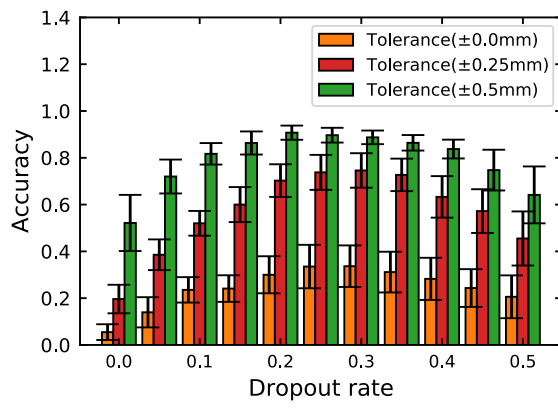
Figure 19

R. Katsuma et. al.

Figure 20

R. Katsuma et. al.

Table I MLP structure details for the 0.25 and 0.5 mm step classifications

	Dropout rate	Activation	No. of units
Input layer	(see Table II)	-	36
hidden layer 1	40%	linear	36
hidden layer 2	40%	relu	400
hidden layer 3	40%	relu	700
hidden layer 4	0%	relu	100
Output layer	-	softmax	9 (0.25 mm step) 17 (0.5 mm step)

Table 1

R. Katsuma et al

Table II Dropout rate at input layer

	Classification scheme	
	0.5 mm	0.25 mm
Artifical defect	0.2	0.25
Actual defect	0.1	0.25

Table 2

R. Katsuma et. al.

Table III Adam parameters

α	0.001
β_1	0.9
β_2	0.999
ε	10^{-8}

Table 3

R. Katsuma et. al.

Table IV

	Tolerant width	Circular radius r of aritificial defect			Overall percentage of correct answers
		50 mm	100 mm	200 mm	
0.5-mm-classification scheme	±0 mm	6/9 (67%)	6/9 (67%)	5/9 (56%)	17/27 (63%)
	±0.5 mm	9/9 (100%)	9/9 (100%)	7/9 (78%)	25/27 (93%)
0.25-mm-classification scheme	±0 mm	5/9 (56%)	4/9 (44%)	4/9 (44%)	13/27 (48%)
	±0.25 mm	9/9 (100%)	6/9 (67%)	6/9 (67%)	21/27 (78%)
	±0.5 mm	9/9 (100%)	9/9 (100%)	6/9 (67%)	24/27 (89%)

Table. 4

R. Katsuma et al

Table V

	Tolerant width	Overall percentage of correct answers
0.5-mm-classification scheme	±0 mm	9/12 (75%)
	±0.5 mm	12/12 (100%)
0.25-mm-classification scheme	±0 mm	3/12 (25%)
	±0.25 mm	9/12 (75%)
	±0.5 mm	12/12 (100%)

Table. 5

R. Katsuma et al